NANO LETTERS

pubs.acs.org/NanoLett Letter

Molten-Salt-Assisted Synthesis of Bismuth Catalysts with Rich Grain Boundaries for Efficient CO_2 Conversion to High-Purity Formic Acid

Laihao Luo,[▽] Qinlong Gao,[▽] Haoyuan Wang, Chunxiao Liu, Yuan Ji, Xu Li, Qiu Jiang, Tingting Zheng,* and Chuan Xia*

Cite This: https://doi.org/10.1021/acs.nanolett.5c03829 Read Online

ACCESS | Metrics & More | Article Recommendations | Supporting Information

ABSTRACT: Electrochemical CO_2 reduction to formic acid, powered by renewable electricity, enables a sustainable carbon cycle by providing a versatile chemical feedstock and energy carrier. Bismuth-based catalysts are known for their high formate selectivity but face challenges in balancing selectivity and stability at industrial current densities. In this study, we present a two-step approach that combines molten-salt synthesis with in situ reduction to fabricate polycrystalline bismuth catalysts with rich exposed grain boundaries (GB-Bi). The GB-Bi catalysts demonstrate exceptional CO_2RR performance, achieving a Faradaic efficiency exceeding 90% toward formate at ampere-level current densities. Spectroscopic evidence combined with theoretical calculations validated the role of grain boundaries in promoting CO_2 adsorption and activation, thereby enhancing the overall catalytic performance. Moreover, when deployed in a solid-state electrolyte reactor, GB-Bi demonstrated outstanding stability, continuously producing a high-purity formic acid solution at −200 mA for over 210 h.

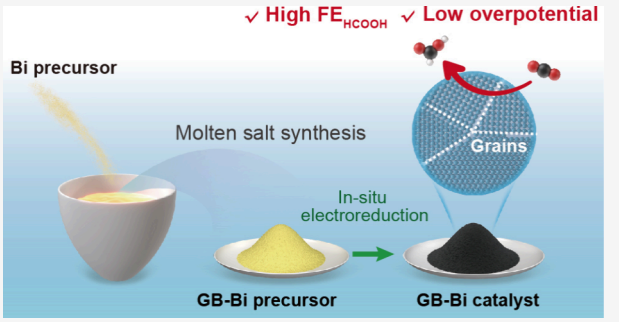

KEYWORDS: *CO_2 electroreduction, bismuth, grain boundary, formic acid, solid-state electrolyte reactor*

By leveraging surplus renewable electricity, the electrochemical reduction of CO_2 (CO_2RR) enables the conversion of CO_2 into a spectrum of high-value chemicals and fuels, contributing to the reduction of CO_2 emissions and facilitating the establishment of a circular carbon economy.[1−6] Among the various products of the CO_2RR, formic acid (HCOOH) has emerged as a particularly compelling target because of its high energy density, nontoxic nature, and easy storage.[7−9] As a versatile chemical intermediate, formic acid plays a crucial role in applications such as hydrogen storage, direct formic acid fuel cells, and pharmaceutical synthesis.[10,11] Additionally, techno-economic analysis suggests that formic acid is among the most economically and technically viable products of the CO_2RR, with the highest profitability per electron transferred.[12] These findings underscore the vast potential of CO_2-to-formic acid conversion for large-scale industrial deployment, bridging renewable energy integration with chemical manufacturing.[13,14]

The CO_2RR process typically begins with the adsorption and activation of CO_2 on the catalyst surface, followed by a sequence of electron transfer and proton-coupled steps that yield intermediates such as *OCHO or *COOH.[15] The nature of these intermediates dictates the selectivity of the reaction toward the desired products; for example, *OCHO intermediates lead to the formation of HCOOH, whereas alternative pathways may direct the reaction toward carbon monoxide (CO), methane (CH_4), or multicarbon (C_{2+}) products.[16,17] However, the high thermodynamic stability of CO_2 molecules and the competitive hydrogen evolution reaction (HER) present significant challenges in achieving efficient and selective CO_2 reduction.[18] This necessitates the development of advanced catalysts that can effectively lower the activation barriers and direct the reaction pathway toward the desired products.[19−21]

Bismuth (Bi)-based catalysts have garnered considerable attention as promising candidates for CO_2-to-formate conversion, because of their environmental friendliness, low toxicity, and inherent selectivity toward formate.[22] Additionally, their low activity for the competing HER makes them particularly advantageous in aqueous systems.[23] Despite these advantages, Bi-based catalysts are hindered by their relatively low catalytic activity, suboptimal partial current density for formate production (j_{HCOOH}), and limited operational stability.[24−26] These challenges arise primarily from the modest kinetics of CO_2 activation on Bi surfaces and structural

Received: July 24, 2025
Revised: August 29, 2025
Accepted: September 2, 2025

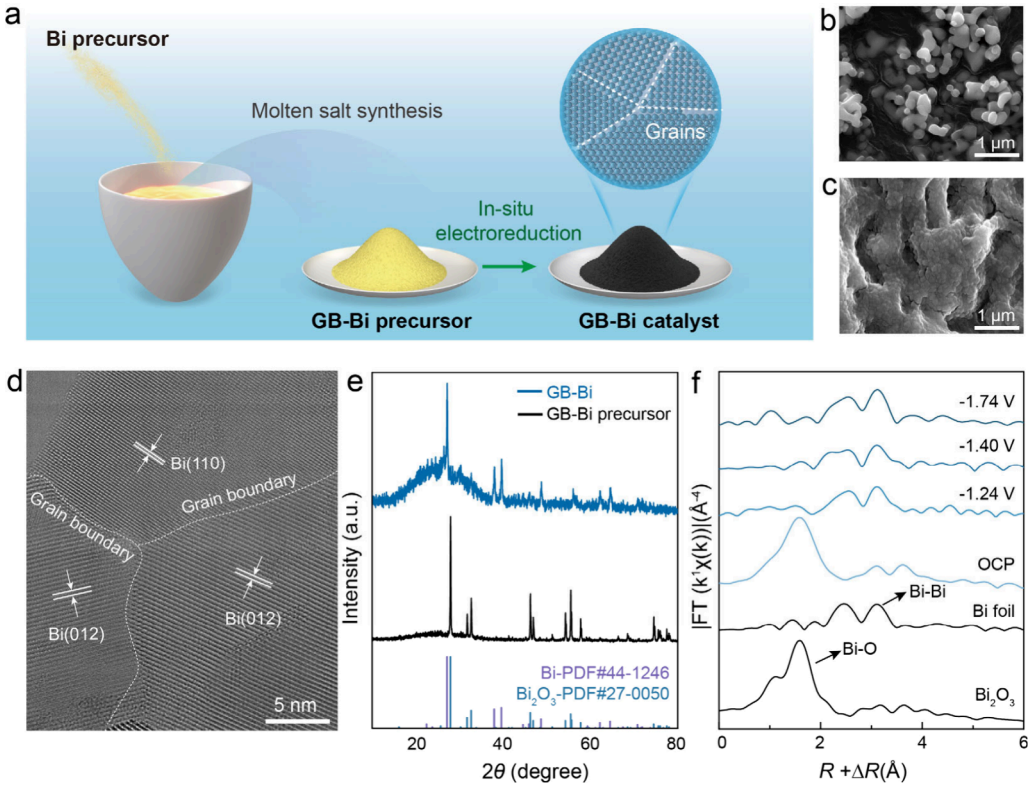

Figure 1. Structural characterization of the GB-Bi catalyst. (a) Schematic illustration of the synthetic process for the GB-Bi catalyst. (b) SEM image of the GB-Bi precursor. (c) SEM image of the GB-Bi precursor after electroredcution. (d) HRTEM image of the GB-Bi catalyst. (e) XRD patterns of the GB-Bi precursor and GB-Bi catalyst. (f) In-situ EXAFS spectra at the Bi L_3-edge of GB-Bi catalysts under formate evolution conditions. The Bi_2O_3 and Bi metal are shown as references. All the potentials were calibrated to the RHE scale.

degradation during prolonged operation. This presents significant barriers to the large-scale industrial application of Bi-based catalysts, and approaches to increase their intrinsic activity and durability are needed.

Recent advances in defect engineering have demonstrated that introducing grain boundaries (GBs) can significantly enhance catalytic performance by providing abundant active sites and improving the adsorption and activation of reaction intermediates.[4,27−29] For example, a high density of GBs in metallic copper (Cu) supports a high density of active undercoordinated sites, which improves the C_{2+} selectivity of 7 nm Cu nanoparticles (NPs).[30] Adding GBs to Au nanoparticles can significantly increase the catalytic activity for CO production.[31] Generally, a nonequilibrium crystallization process favors the enrichment of GBs, and strategies including annealing precursors in specific atmospheres, pulsed laser ablation, and steam treatment have been developed accordingly.[32−34] However, replicating these methods for the synthesis of GB-rich Bi catalysts is challenging. Owing to the low melting point of Bi and its aerobic nature, controlling its structural evolution is particularly difficult.[35] Recently, strategies such as high-pressure treatment and rapid thermal shock have been employed to introduce GBs into Bi-based catalysts.[36,37] Nevertheless, these methods demand specialized equipment and face scalability challenges.

In this work, we report the development of polycrystalline Bi catalysts with rich exposed grain boundaries (GB-Bi) through a two-step process that combines molten salt synthesis and in-situ reduction during the CO_2RR. This approach uses the simplicity, scalability, and nonequilibrium advantages of the molten salt method to synthesize uniform-sized Bi oxide nanoparticle precursors, which facilitate the aggregation and formation of abundant grain boundaries during the subsequent reduction process. The resulting GB-Bi catalysts demonstrate outstanding performance in the CO_2RR, enabling high activity for formate production at −1 A cm^{-2} with a Faradaic efficiency (FE) of ∼95%. When integrated into a solid-state electrolytic reactor, GB-Bi enables the continuous production of a high-purity formic acid solution at −200 mA for 214 h. In-situ spectroscopic analysis and theoretical calculations reveal that the grain boundaries enhance the adsorption and activation of key intermediates (*CO_2 and *OCHO), significantly increasing the catalytic performance.

The molten salt synthetic method serves widely as an efficient way to fabricate nanomaterials with uniform geometric structures.[38] As reported, molten salts provide not only a uniform liquid environment at high temperatures but also strong polarity forces, which create favorable conditions for nucleation and attachment.[39,40] In light of these advantages, we intended to introduce grain boundaries in Bi through a two-step strategy, as shown in Figure 1a.

Initially, the molten salt synthetic step enables the production of GB-Bi precursors with a uniform size of approximately 200 nm, as revealed by scanning electron microscopy (SEM) and transmission electron microscopy (TEM) characterization (see Figure 1b, as well as Figures S1 and S2). Driven by strong polarity forces, these nanoparticles adhere to each other, providing multiple interfaces for grain formation. The follow-up in-situ electroreduction of the precursors under CO_2RR conditions at a constant current density of −300 mA cm^{-2} yields the GB-Bi catalyst. SEM images indicate that severe coalescence of the nanoparticles

https://doi.org/10.1021/acs.nanolett.5c03829
Nano Lett. XXXX, XXX, XXX−XXX

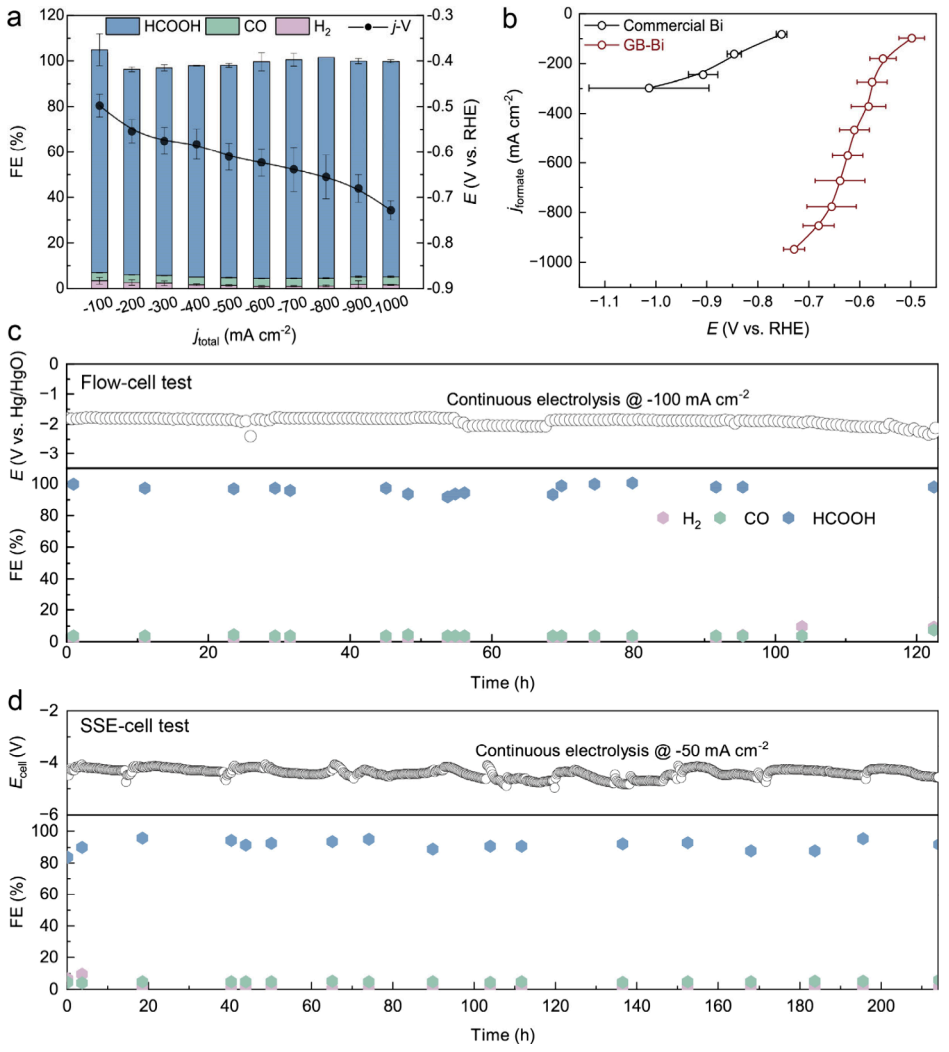

Figure 2. CO_2RR performance of the GB-Bi catalyst. (a) FEs of all products at different current densities and the corresponding $j-V$ curves of the GB-Bi catalyst. (b) Partial current density of $HCOO^-$ under different applied potentials for GB-Bi and commercial Bi. (c) Stability test at a constant current density of -100 mA cm^{-2} in a flow cell. (d) Stability test at a constant current density of -50 mA cm^{-2} in a solid-state electrolyte reactor.

occurred after electroreduction (Figure 1c). The abundance of the grain boundaries was also evidenced by high-resolution transmission electron microscopy (HRTEM) (Figure 1d). The lattice fringes with interplanar spacings of 0.32 and 0.23 nm were assigned to the (012) and (110) facets of rhombohedral Bi, respectively. These lattice fringes containing multiple orientations were clearly interconnected by grain boundaries. X-ray diffraction (XRD) analysis revealed that the GB-Bi precursors are mainly composed of the Bi_2O_3 phase, revealing its transformation into metallic Bi after electroreduction (Figure 1e).

We also verified the phase transfer under CO_2RR conditions through in-situ X-ray absorption spectroscopy (XAS) studies. As shown in Figure 1f, the spectrum of the GB-Bi precursor exhibited Bi−O paths closely matching those of Bi_2O_3 at the open circuit potential (OCP). Upon the application of reductive potentials, the scattering feature corresponding to the Bi−O paths diminished. Two peaks associated with the Bi−Bi paths in metallic Bi arise, indicating the transformation of Bi_2O_3 into metallic Bi under CO_2RR conditions. These results correspond well with the TEM and XRD results, indicating the successful fabrication of a grain-boundary-rich Bi catalyst through the combination of molten salt synthesis and in-situ electroreduction.

We evaluated the CO_2 reduction reaction (CO_2RR) performance of the GB-Bi catalyst with a conventional three-electrode flow-cell setup (Figure S3; see the Supporting Information for details). A 1 M KOH solution was used as the electrolyte. Anion chromatography was employed to analyze the liquid products, and gas chromatography (GC) was used for gaseous product identification. Linear sweep voltammetry (LSV) measurements revealed a dramatic increase in current density under a CO_2 atmosphere compared with a N_2 atmosphere (Figure S4), indicating that GB-Bi has more favorable activity toward the CO_2RR than toward the HER. During the CO_2RR, the GB-Bi catalyst predominantly produces formate as the liquid product, with negligible amounts of CO and H_2 (<3%). At a potential of −0.50 V versus the reversible hydrogen electrode (vs. RHE), the partial current density for formate ($j_{formate}$) reached −98.0 mA cm^{-2}, achieving a maximum formate Faradaic efficiency ($FE_{formate}$) of approximately 97% (Figure 2a). Across the applied potential range from −0.50 to −0.73 V vs. RHE, the $FE_{formate}$ consistently exceeded 90%, whereas the FE_{H2} was suppressed

https://doi.org/10.1021/acs.nanolett.5c03829
Nano Lett. XXXX, XXX, XXX−XXX

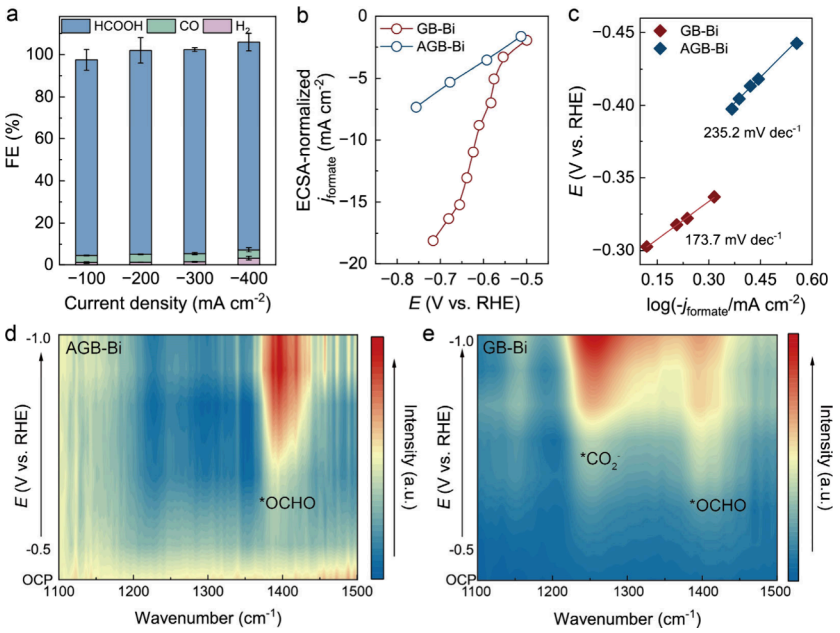

Figure 3. Mechanistic studies. (a) FEs of all products at different current densities over AGB-Bi. (b) ECSA-normalized partial current densities for formate. (c) Tafel plots for formate production over GB-Bi and AGB-Bi. (d) In-situ ATR-SEIRAS spectra during the CO_2RR over AGB-Bi in a potential window from −0.5 V to −1.0 V. (e) In-situ ATR-SEIRAS spectra during the CO_2RR over GB-Bi in a potential window from −0.5 V to −1.0 V.

to less than 3%. Notably, GB-Bi achieved a high activity up to −1 A cm^{-2} at approximately −0.73 V vs. RHE while maintaining an $FE_{formate}$ of ∼95%. In comparison, commercial bismuth nanoparticles (Figures S5 and S6) presented a limited $FE_{formate}$ of ∼80%, and a much higher overpotential is required to drive CO_2-to-formate conversion (see Figure 2b, as well as Figure S7). This high-performance CO_2-to-formate conversion by GB-Bi surpasses the performance of previously reported state-of-the-art Bi-based electrocatalysts in alkaline electrolytes (see Figure S8 and Tables S1 and S2).[26,41−46] Moreover, we evaluated the long-term stability of GB-Bi in a flow cell at a constant current density of −100 mA cm^{-2}. Strikingly, the results show that GB-Bi maintained an $FE_{formate}$ exceeding 90% after 122 h of operation (Figure 2d), which is also superior to that of previously reported Bi-based catalysts (see Figure S9 and Table S3).[15,41,43−45,47−49]

Generally, it is believed that the applied negative potential triggers the reduction of bismuth oxide precursors and the reconstruction of the catalyst structure with the elimination of lattice oxygen. The structural properties of the precursors and the reduction conditions are two main aspects that affect the formation of GBs. To investigate the influence of the precursor structure, we varied the annealing duration (1, 2, and 4 h) for the molten-salt treatment, which is believed to affect the grain size of the Bi_2O_3 precursor and the density of oxygen vacancies. As shown in Figures S10a and S10b, increasing the annealing duration increased both the grain size of the Bi_2O_3 precursor (from 47.6 nm to 66.3 nm) and the oxygen vacancy content (from 59.8% to 69.0%). For precursors of different annealing durations, the reduction current was fixed at −300 mA cm^{-2}. As revealed in Figure S10c, these variations, in turn, lead to an increased overpotential for HCOOH production. These results highlight the importance of the structural properties of the precursor for rich GB formation. We suspect that a larger grain size decreases the GB density and that a greater content of oxygen vacancies increases the mobility of the lattice oxygen, which would facilitate the reduction process of Bi_2O_3 to Bi and the rearrangement of Bi atoms to an energetically stable state.[50]

A violent prereduction condition also favors the generation of a high-energy metastable GB structure.[33,51] As shown in Figure S10d, the GB-Bi catalyst prereduced at a lower current density (−150 mA cm^{-2}) exhibited a slightly larger overpotential for formate production. Indeed, it is reported that the density of GBs can be easily tuned by the reduction potential, and a more negative reduction potential results in a higher GB density.[33] A larger prereduction current density or a more negative potential provides additional driving forces and energy for stabilizing the metastable GB structure.

The resulting formate product from the CO_2RR using a conventional flow-cell setup is generally mixed with electrolyte salts (e.g., KOH). Additional separation and purification processes are required to obtain formate salt or formic acid in high purity.[47,48] These steps significantly increase energy consumption and operational costs, posing a major obstacle to the commercialization of CO_2RR techniques. To address this issue, we implanted the GB-Bi catalyst into a solid-state electrolyte reactor (SSE), as we previously developed, to realize the direct production of electrolyte-free formic acid.[49] A schematic illustration of the structure of the SSE is provided in Figure S11. Once CO_2 is reduced into $HCOO^-$ at the cathode side, driven by the electric field, the negatively charged $HCOO^-$ travels through the anion exchange membrane into the middle solid-electrolyte layer. At the same time, the protons (H^+) generated by water oxidation at the anode side move across the cation exchange membrane to compensate for the charge. The HCOOH formed through the combination of $HCOO^-$ and H^+ in the middle solid-electrolyte layer is then released by the deionized water stream. Remarkably, the integration of the GB-Bi catalyst and SSE reactor resulted in stable production of a pure formic acid solution at a fixed current density of −50 mA cm^{-2} (200 mA) for 214 h (see

https://doi.org/10.1021/acs.nanolett.5c03829
Nano Lett. XXXX, XXX, XXX−XXX

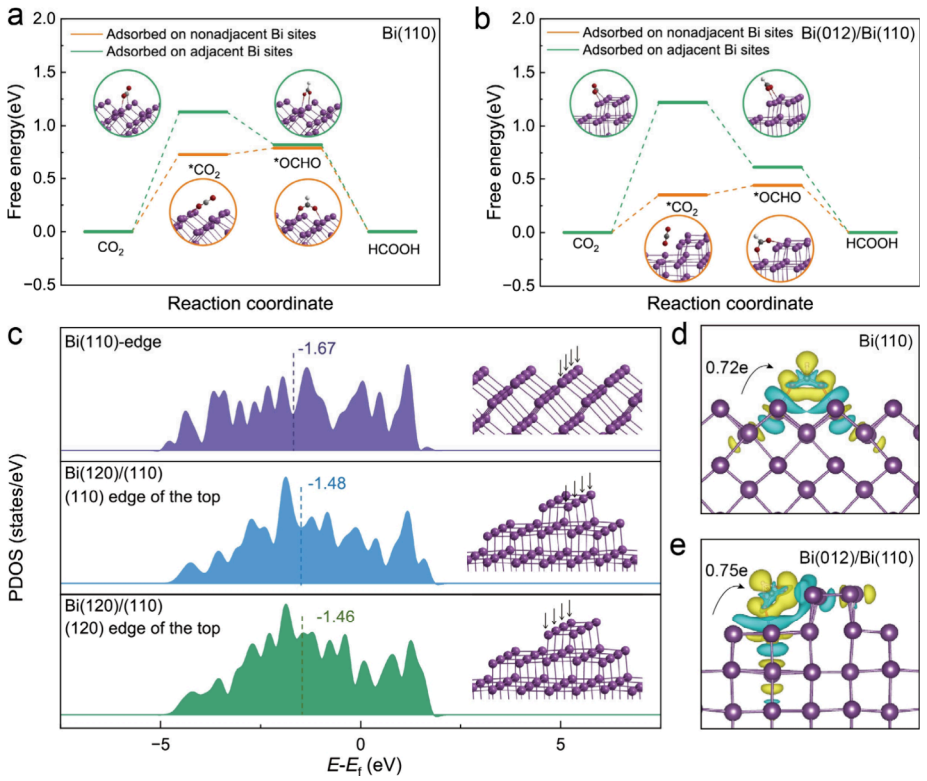

Figure 4. DFT calculations. (a) Free-energy profiles of the CO_2RR to formate on Bi(110). (b) Free-energy profiles of the CO_2RR to formate on the Bi(012) edge of Bi(012)/Bi(110). The insets show the optimized adsorption configurations of the intermediates, where Bi, O, C, and H atoms are presented in purple, red, gray, and white, respectively. (c) PDOS of Bi 2p in the Bi(110) and Bi(012)/Bi(110) models. (d) Charge density difference plots of *OCHO adsorbed on Bi(110) models. (e) Charge density difference plots of *OCHO adsorbed on Bi(012)/Bi(110) models.

Figure 2d, as well as Figures S12−S14). The FE_{HCOOH} remained higher than 80%.

We further revealed the impact of grain boundaries on the CO_2RR performance. As reported previously, thermal annealing has been proposed as an efficient method to eliminate grain boundaries.[31] We annealed GB-Bi at 320 °C for 4 h in an argon atmosphere and obtained a grain-boundary-free Bi catalyst (denoted as AGB-Bi). SEM images revealed that AGB-Bi retained the morphology of GB-Bi after the annealing process, featuring abundant particle aggregations (Figure S15). HRTEM analysis revealed that metallic Bi(110) facets dominated AGB-Bi, and negligible grain boundaries were observed (Figure S16). CO_2RR tests performed in a flow cell revealed that although AGB-Bi exhibited high FE_{HCOOH} (≥95%) toward the CO_2RR, its activity was significantly constrained at high overpotential regions, compared with that of GB-Bi (see Figure 3a, as well as Figure S17). Even after excluding the influence of differences in the electrochemically active surface area (ECSA), GB-Bi exhibited an enhanced intrinsic CO_2RR performance compared with that of AGB-Bi, highlighting the critical role of grain boundaries (see Figure 3b, as well as Figure S18). To gain deeper insights into the impact of grain boundaries on CO_2RR kinetics, we performed Tafel slope analysis. As shown in Figure 3c, GB-Bi and AGB-Bi exhibited Tafel slopes of 173.7 and 235.2 mV dec^{-1}, respectively. Generally, it is believed that these large Tafel slopes (≥118 mV dec^{-1}) indicate that the first electron transfer to CO_2 is the rate-determining step (RDS).[52] GB-Bi displayed a smaller Tafel slope than AGB-Bi did, which indicates facilitated electron transfer kinetics and CO_2 activation capability in the presence of grain boundaries.[53]

We also conducted in-situ attenuated total reflection surface-enhanced infrared absorption spectroscopy (ATR-SEIRAS) experiments to monitor the reactive intermediates generated during the CO_2RR on GB-Bi and AGB-Bi. As shown in Figures 3d and 3e, a characteristic infrared band located at approximately 1400 cm^{-1} was observed for both GB-Bi and AGB-Bi. This band can be assigned to the vibration of O−C−O in the adsorbed *OCHO intermediate, with the oxygen side adsorbed on the catalyst surface.[54,55] In contrast, negligible bands were found in the range of 1900−2100 cm^{-1} over GB-Bi, indicating the weak adsorption of CO* intermediates on the surface (Figure S19).[56] These observations are consistent with previously reported works, which propose that $HCOO^-$ is generated through the hydrogenation of C atoms by forming *OCHO intermediates and that CO is generated through the hydrogenation of O atoms and cleavage of C−O bonds by the formation of CO* intermediates. Interestingly, GB-Bi exhibited a pronounced increase in the intensity of the band at approximately 1250 cm^{-1} with increasing overpotential (Figure 3d). This band can be assigned to asymmetric $-COO^-$ stretching of activated $*CO_2^-$ species;[42,57,58] however, it was not detected on AGB-Bi throughout the potential range, further indicating that GB-Bi is more favorable for CO_2 adsorption and activation. These findings align with the Tafel slope analysis, indicating that the grain boundaries in GB-Bi significantly enhance its ability to adsorb and activate $*CO_2^-$.

We further performed isotope labeling experiments to reveal the impact of GBs on the hydrogenation process in CO_2-to-HCOOH conversion. As shown in Figure S20, the GB-free AGB-Bi catalyst exhibits a primary KIE value of ∼1.4,

https://doi.org/10.1021/acs.nanolett.5c03829
Nano Lett. XXXX, XXX, XXX−XXX

indicating that the dissociation of water is involved in the rate-determining step for formate production. The GB-Bi catalyst exhibited a much larger KIE value of ~2.0, indicating more sluggish kinetics for water activation, and the HCOOH production rate was highly dependent on protonation steps.[59,60] This phenomenon consists of improved CO_2 activation on the GB-Bi surface compared with that on the AGB-Bi surface, as evidenced by the above in-situ infrared characterization. Apparently, the presence of GBs exerts a greater effect on enhancing CO_2 activation than on inhibiting water dissociation.

Density functional theory (DFT) calculations were further performed to elucidate the influence of the grain boundaries on the reaction path. On the basis of the HRTEM analysis, we considered the CO_2RR on the surfaces of Bi(110), Bi(012), and the boundaries of Bi(012)/Bi(110) and Bi(012)/Bi(012). Figures 4a-4b depict the reaction path for CO_2-to-HCOOH conversion on Bi(110) and Bi(012)/Bi(110). Both the monodentate and bidentate adsorption configurations of $*CO_2$ are considered. On the basis of the calculation results, the activation of CO_2 with the highest Gibbs free energy increase was identified as the rate-determining step, which is consistent with the Tafel analysis results. The Gibbs free energy for $*CO_2$ formation on the Bi(012)/Bi(110) grain boundary was found to be 0.35 eV (Figure 4b), which was significantly lower than that on the Bi(110) edge (0.41 eV), Bi(110) surface (0.73 eV), or Bi(012) surface (0.58 eV) (see Figure 4a, as well as Figures S21 and S22). The lowest Gibbs free energy for $*CO_2$ formation (0.27 eV) was found at the Bi(012)/Bi(012) boundaries, considering that CO_2 was adsorbed on nonadjacent Bi sites (Figure S23). The hydrogenation of $*CO_2$ to *OCHO is energetically favorable, which requires a tiny Gibbs free-energy increase or even show negative changes (see Figures 4a and 4b, as well as Figures S21−S23).

We further analyzed the projected density of states (PDOS) and *p*-band centers on different Bi sites to provide electronic insights into the benefit of boundary sites on the adsorption of key intermediates (Figure 4c). Apparently, the *p*-band center for Bi sties on the top (012) edge of the Bi(012)/Bi(110) boundary (−1.46 eV) is closer to the Fermi level than the *p*-band center for Bi sties on the top (011) edge (−1.48 eV) and plain Bi(110) surface (−1.67 eV). As reported previously, the upshift of the *p*-band center could facilitate *OCHO formation through *p*−*p* hybridization. Further Bader charge analysis revealed enhanced interactions between boundary sites and *OCHO adsorbers. As shown in Figures 4d and 4e, more electrons are transferred to *OCHO at the Bi(012)/Bi(110) boundary (0.75 e) than at the Bi(110) surface (0.72 e), which correlates with a lower Gibbs free energy for the adsorption of the *OCHO intermediate at the Bi(012)/Bi(110) boundary (Figure 4b). The interaction on the Bi(012)/Bi(012) boundary was also greater than that on the plain Bi(012) surface (Figure S24). Overall, these results provide compelling evidence that the presence of grain boundaries significantly enhances the CO_2 activation and *OCHO formation processes by optimizing the electronic structure and lowering the activation barriers.

In summary, we have demonstrated an effective two-step synthetic strategy for introducing rich grain boundaries into Bi catalysts. The obtained GB-Bi catalyst demonstrates excellent performance in CO_2-to-HCOOH conversion, achieving FE_{HCOOH} values exceeding 90% at ampere-level current densities. Experimental and theoretical analyses have suggested that the grain boundaries in GB-Bi significantly enhance CO_2 activation by modulating the adsorption energy of intermediates and accelerating electron transfer processes. The integration of GB-Bi catalysts with a solid-state electrolyte reactor enabled long-term production of high-purity formic acid for over 210 h at a constant current of −200 mA. This work highlights the pivotal role of grain boundaries in enhancing catalytic performance and opens up an appealing approach to fabricate grain boundary rich catalysts for the CO_2RR.

■ ASSOCIATED CONTENT

Supporting Information

The Supporting Information is available free of charge at https://pubs.acs.org/doi/10.1021/acs.nanolett.5c03829.

Additional structural characterizations; CO_2RR measurements; performance comparison; construction of models and computation results (PDF)

■ AUTHOR INFORMATION

Corresponding Authors

Tingting Zheng − *School of Materials and Energy, University of Electronic Science and Technology of China, Chengdu, Sichuan 611731, P. R. China*; Email: ttzheng@uestc.edu.cn

Chuan Xia − *Yangtze Delta Region Institute (Huzhou), University of Electronic Science and Technology of China, Huzhou, Zhejiang 313001, P. R. China; School of Materials and Energy, University of Electronic Science and Technology of China, Chengdu, Sichuan 611731, P. R. China*; orcid.org/0000-0003-4526-159X; Email: chuan.xia@uestc.edu.cn

Authors

Laihao Luo − *Yangtze Delta Region Institute (Huzhou), University of Electronic Science and Technology of China, Huzhou, Zhejiang 313001, P. R. China; School of Materials and Energy, University of Electronic Science and Technology of China, Chengdu, Sichuan 611731, P. R. China*; orcid.org/0009-0000-0421-088X

Qinlong Gao − *School of Materials and Energy, University of Electronic Science and Technology of China, Chengdu, Sichuan 611731, P. R. China*

Haoyuan Wang − *School of Materials and Energy, University of Electronic Science and Technology of China, Chengdu, Sichuan 611731, P. R. China*

Chunxiao Liu − *School of Materials and Energy, University of Electronic Science and Technology of China, Chengdu, Sichuan 611731, P. R. China*

Yuan Ji − *School of Materials and Energy, University of Electronic Science and Technology of China, Chengdu, Sichuan 611731, P. R. China*

Xu Li − *School of Materials and Energy, University of Electronic Science and Technology of China, Chengdu, Sichuan 611731, P. R. China*; orcid.org/0000-0001-7577-4957

Qiu Jiang − *Yangtze Delta Region Institute (Huzhou), University of Electronic Science and Technology of China, Huzhou, Zhejiang 313001, P. R. China; School of Materials and Energy, University of Electronic Science and Technology of China, Chengdu, Sichuan 611731, P. R. China*; orcid.org/0000-0002-2408-198X

https://doi.org/10.1021/acs.nanolett.5c03829
Nano Lett. XXXX, XXX, XXX−XXX

Complete contact information is available at:
https://pubs.acs.org/10.1021/acs.nanolett.5c03829

Author Contributions

[▽]Authors L. Luo and Q. Gao contributed equally to this work.

Notes

The authors declare no competing financial interest.

■ ACKNOWLEDGMENTS

We acknowledge the "Pioneer" and "Leading Goose" R&D Program of Zhejiang (Grant No. 2023C03017), the National Natural Science Foundation of China (Nos. 22322201, 52171201, 22278067, 22309171, 22301031), the Natural Science Foundation of Sichuan Province (Nos. 2025NSFJQ0017, 2023NSFSC0911), and the Key Science & Technology Project of Anhui Province (202423110050009). We thank beamline BL11B (31124.02.SSRF.BL11B) of the Shanghai Synchrotron Radiation Facility for providing the facilities for XAFS analysis. We appreciate the Analysis and Testing Center, University of Electronic Science and Technology of China, for their technical support.

■ REFERENCES

(1) Fan, L.; Xia, C.; Yang, F.; Wang, J.; Wang, H.; Lu, Y. Strategies in catalysts and electrolyzer design for electrochemical CO_2 reduction toward C_{2+} products. *Sci. Adv.* **2020**, *6*, eaay3111.

(2) Nitopi, S.; Bertheussen, E.; Scott, S. B.; Liu, X.; Engstfeld, A. K.; Horch, S.; Seger, B.; Stephens, I. E. L.; Chan, K.; Hahn, C.; Nørskov, J. K.; Jaramillo, T. F.; Chorkendorff, I. Progress and perspectives of electrochemical CO_2 reduction on copper in aqueous electrolyte. *Chem. Rev.* **2019**, *119*, 7610−7672.

(3) Abdelkader-Fernández, V. K.; Fernandes, D. M.; Freire, C. Carbon-based electrocatalysts for CO_2 electroreduction produced via MOF, biomass, and other precursors carbonization: A review. *J. CO_2 Util.* **2020**, *42*, 101350.

(4) Yu, J.; Wang, J.; Ma, Y.; Zhou, J.; Wang, Y.; Lu, P.; Yin, J.; Ye, R.; Zhu, Z.; Fan, Z. Recent progresses in electrochemical carbon dioxide reduction on copper-based catalysts toward multicarbon products. *Adv. Funct. Mater.* **2021**, *31*, 2102151.

(5) Saha, P.; Amanullah, S.; Dey, A. Selectivity in electrochemical CO_2 reduction. *Acc. Chem. Res.* **2022**, *55*, 134−144.

(6) Lai, W.; Qiao, Y.; Zhang, J.; Lin, Z.; Huang, H. Design strategies for markedly enhancing energy efficiency in the electrocatalytic CO_2 reduction reaction. *Energy Environ. Sci.* **2022**, *15*, 3603−3629.

(7) Han, N.; Ding, P.; He, L.; Li, Y.; Li, Y. Promises of main group metal-based nanostructured materials for electrochemical CO_2 reduction to formate. *Adv. Energy Mater.* **2020**, *10*, 1902338.

(8) Qiao, Y.; Lai, W.; Huang, K.; Yu, T.; Wang, Q.; Gao, L.; Yang, Z.; Ma, Z.; Sun, T.; Liu, M.; Lian, C.; Huang, H. Engineering the local microenvironment over Bi nanosheets for highly selective electrocatalytic conversion of CO_2 to HCOOH in strong acid. *ACS Catal.* **2022**, *12*, 2357−2364.

(9) Liu, S.; Xiao, J.; Lu, X. F.; Wang, J.; Wang, X.; Lou, X. W. Efficient electrochemical reduction of CO_2 to HCOOH over sub-2 nm SnO_2 quantum wires with exposed grain boundaries. *Angew. Chem., Int. Ed.* **2019**, *58*, 8499−8503.

(10) Mustafa, A.; Lougou, B. G.; Shuai, Y.; Razzaq, S.; Wang, Z.; Shagdar, E.; Zhao, J. A techno-economic study of commercial electrochemical CO_2 reduction into diesel fuel and formic acid. *J. Electrochem. Sci. Technol.* **2022**, *13*, 148−158.

(11) Pérez-Fortes, M.; Schöneberger, J. C.; Boulamanti, A.; Harrison, G.; Tzimas, E. Formic acid synthesis using CO_2 as raw material: Techno-economic and environmental evaluation and market potential. *Int. J. Hydrogen Energy* **2016**, *41*, 16444−16462.

(12) Rodríguez-Varela, J.; Alonso-Lemus, I. L.; Savadogo, O.; Palaniswamy, K. Overview: Current trends in green electrochemical energy conversion and storage. *J. Mater. Res.* **2021**, *36*, 4071−4083.

(13) Zhang, C.; Hao, X.; Wang, J.; Ding, X.; Zhong, Y.; Jiang, Y.; Wu, M.-C.; Long, R.; Gong, W.; Liang, C.; et al. Concentrated formic acid from CO_2 electrolysis for directly driving fuel cell. *Angew. Chem., Int. Ed.* **2024**, *63*, e202317628.

(14) Kuang, Y.; Rabiee, H.; Ge, L.; Rufford, T. E.; Yuan, Z.; Bell, J.; Wang, H. High-concentration electrosynthesis of formic acid/formate from CO_2: Reactor and electrode design strategies. *Energy Environ. Mater.* **2023**, *6*, e12596.

(15) Li, Z.; Sun, B.; Xiao, D.; Wang, Z.; Liu, Y.; Zheng, Z.; Wang, P.; Dai, Y.; Cheng, H.; Huang, B. Electron-rich Bi nanosheets promote $CO_2^{\bullet-}$ formation for high-performance and pH-universal electrocatalytic CO_2 reduction. *Angew. Chem., Int. Ed.* **2023**, *62*, e202217569.

(16) Lei, Y.; Wang, Z.; Bao, A.; Tang, X.; Huang, X.; Yi, H.; Zhao, S.; Sun, T.; Wang, J.; Gao, F. Recent advances on electrocatalytic CO_2 reduction to resources: Target products, reaction pathways and typical catalysts. *Chem. Eng. J.* **2023**, *453*, 139663.

(17) Li, Z.; Li, B.; Yu, M.; Yu, C.; Shen, P. Amorphous metallic ultrathin nanostructures: A latent ultra-high-density atomic-level catalyst for electrochemical energy conversion. *Int. J. Hydrogen Energy* **2022**, *47*, 26956−26977.

(18) Lei, P.-X.; Liu, S.-Q.; Wen, Q.-R.; Wu, J.-Y.; Wu, S.; Wei, X.; Feng, R.; Fu, X.-Z.; Luo, J.-L. Integrated "two-in-one" strategy for high-rate electrocatalytic CO_2 reduction to formate. *Angew. Chem., Int. Ed.* **2025**, *64*, e202415726.

(19) Gao, Q.; Wang, H.; Liu, C.; Luo, L.; Li, X.; Jiang, Q.; Ji, Y.; Zheng, T.; Xia, C. Regulatory mechanisms and applications of rare earth elements-based electrocatalysts. *Chin. J. Chem.* **2025**, *43*, 205−218.

(20) Jiang, M.; Wang, H.; Zhu, M.; Luo, X.; He, Y.; Wang, M.; Wu, C.; Zhang, L.; Li, X.; Liao, X.; Jiang, Z.; Jin, Z. Review on strategies for improving the added value and expanding the scope of CO_2 electroreduction products. *Chem. Soc. Rev.* **2024**, *53*, 5149−5189.

(21) Han, J.; Bai, X.; Xu, X.; Bai, X.; Husile, A.; Zhang, S.; Qi, L.; Guan, J. Advances and challenges in the electrochemical reduction of carbon dioxide. *Chem. Sci.* **2024**, *15*, 7870−7907.

(22) Xia, D.; Yu, H.; Xie, H.; Huang, P.; Menzel, R.; Titirici, M. M.; Chai, G. Recent progress of Bi-based electrocatalysts for electrocatalytic CO_2 reduction. *Nanoscale* **2022**, *14*, 7957−7973.

(23) Yang, C.; Chai, J.; Wang, Z.; Xing, Y.; Peng, J.; Yan, Q. Recent progress on bismuth-based nanomaterials for electrocatalytic carbon dioxide reduction. *Chem. Res. Chin. Univ.* **2020**, *36*, 410−419.

(24) Gong, Q.; Ding, P.; Xu, M.; Zhu, X.; Wang, M.; Deng, J.; Ma, Q.; Han, N.; Zhu, Y.; Lu, J.; et al. Structural defects on converted bismuth oxide nanotubes enable highly active electrocatalysis of carbon dioxide reduction. *Nat. Commun.* **2019**, *10*, 2807.

(25) Feng, X.; Zou, H.; Zheng, R.; Wei, W.; Wang, R.; Zou, W.; Lim, G.; Hong, J.; Duan, L.; Chen, H. Bi_2O_3/BiO_2 nanoheterojunction for highly efficient electrocatalytic CO_2 reduction to formate. *Nano Lett.* **2022**, *22*, 1656−1664.

(26) Lv, L.; Lu, R.; Zhu, J.; Yu, R.; Zhang, W.; Cui, E.; Chen, X.; Dai, Y.; Cui, L.; Li, J.; et al. Coordinating the edge defects of bismuth with sulfur for enhanced CO_2 electroreduction to formate. *Angew. Chem., Int. Ed.* **2023**, *62*, e202303117.

(27) Wang, Y.; Han, P.; Lv, X.; Zhang, L.; Zheng, G. Defect and interface engineering for aqueous electrocatalytic CO_2 reduction. *Joule* **2018**, *2*, 2551−2582.

(28) Xiao, L.; Wang, Z.; Guan, J. Optimization strategies of high-entropy alloys for electrocatalytic applications. *Chem. Sci.* **2023**, *14*, 12850−12868.

(29) Zhao, Z. L.; Wang, Q.; Huang, X.; Feng, Q.; Gu, S.; Zhang, Z.; Xu, H.; Zeng, L.; Gu, M.; Li, H. Boosting the oxygen evolution reaction using defect-rich ultra-thin ruthenium oxide nanosheets in acidic media. *Energy Environ. Sci.* **2020**, *13*, 5143−5151.

(30) Yang, Y.; Louisia, S.; Yu, S.; Jin, J.; Roh, I.; Chen, C.; Fonseca Guzman, M. V.; Feijoo, J.; Chen, P.-C.; Wang, H.; et al. Operando

https://doi.org/10.1021/acs.nanolett.5c03829
Nano Lett. XXXX, XXX, XXX−XXX

studies reveal active Cu nanograins for CO_2 electroreduction. *Nature* **2023**, *614*, 262−269.
(31) Mariano, R. G.; McKelvey, K.; White, H. S.; Kanan, M. W. Selective increase in CO_2 electroreduction activity at grain-boundary surface terminations. *Science* **2017**, *358*, 1187−1192.
(32) Wu, Q.; Du, R.; Wang, P.; Waterhouse, G. I. N.; Li, J.; Qiu, Y.; Yan, K.; Zhao, Y.; Zhao, W.-W.; Tsai, H.-J.; Chen, M.-C.; Hung, S.-F.; Wang, X.; Chen, G. Nanograin-boundary-abundant Cu_2O-Cu nanocubes with high C_{2+} selectivity and good stability during electrochemical CO_2 reduction at a current density of 500 mA/cm^2. *ACS Nano* **2023**, *17*, 12884−12894.
(33) Li, Z.; Wang, Y.; Liu, H.; Feng, Y.; Du, X.; Xie, Z.; Zhou, J.; Liu, Y.; Song, Y.; Wang, F.; Sui, M.; Lu, Y.; Fang, F.; Sun, D. Electroreduction-driven distorted nanotwins activate pure Cu for efficient hydrogen evolution. *Nat. Mater.* **2025**, *24*, 424−432.
(34) Huang, W.; Johnston-Peck, A. C.; Wolter, T.; Yang, W.-C. D.; Xu, L.; Oh, J.; Reeves, B. A.; Zhou, C.; Holtz, M. E.; Herzing, A. A.; Lindenberg, A. M.; Mavrikakis, M.; Cargnello, M. Steam-created grain boundaries for methane C-H activation in palladium catalysts. *Science* **2021**, *373*, 1518−1523.
(35) Zhang, X.; Liu, J.; Deng, Z. Bismuth-based liquid metals: advances, applications, and prospects. *Mater. Horiz.* **2024**, *11*, 1369−1394.
(36) Ruan, S.; Zhang, B.; Zou, J.; Zhong, W.; He, X.; Lu, J.; Zhang, Q.; Wang, Y.; Xie, S. Bismuth nanosheets with rich grain boundaries for efficient electroreduction of CO_2 to formate under high pressures. *Chin. J. Catal.* **2022**, *43*, 3161−3169.
(37) Yang, S.; Wang, H.; Xiong, Y.; Zhu, M.; Sun, J.; Jiang, M.; Zhang, P.; Wei, J.; Xing, Y.; Tie, Z.; Jin, Z. Ultrafast thermal shock synthesis and porosity engineering of 3D hierarchical Cu-Bi nanofoam electrodes for highly selective electrochemical CO_2 reduction. *Nano Lett.* **2023**, *23*, 10140−10147.
(38) Chen, D.; Mu, S. Molten salt-assisted synthesis of catalysts for energy conversion. *Adv. Mater.* **2024**, *36*, No. 2408285.
(39) Liu, Z.; Yang, S.; Sun, B.; Chang, X.; Zheng, J.; Li, X. A peapod-like CoP@C nanostructure from phosphorization in a low-temperature molten salt for high-performance lithium-ion batteries. *Angew. Chem., Int. Ed.* **2018**, *57*, 10187−10191.
(40) Xiao, M.; Zhang, L.; Luo, B.; Lyu, M.; Wang, Z.; Huang, H.; Wang, S.; Du, A.; Wang, L. Molten-salt-mediated synthesis of an atomic nickel co-catalyst on TiO_2 for improved photocatalytic H_2 evolution. *Angew. Chem., Int. Ed.* **2020**, *59*, 7230−7234.
(41) Zhu, J.; Li, J.; Lu, R.; Yu, R.; Zhao, S.; Li, C.; Lv, L.; Xia, L.; Chen, X.; Cai, W.; et al. Surface passivation for highly active, selective, stable, and scalable CO_2 electroreduction. *Nat. Commun.* **2023**, *14*, 4670.
(42) Zeng, G.; He, Y.; Ma, D.-D.; Luo, S.; Zhou, S.; Cao, C.; Li, X.; Wu, X.-T.; Liao, H.-G.; Zhu, Q.-L. Reconstruction of Ultrahigh-aspect-ratio crystalline bismuth-organic hybrid nanobelts for selective electrocatalytic CO_2 Reduction to Formate. *Adv. Funct. Mater.* **2022**, *32*, 2201125.
(43) Liu, Y.; Wei, Z.; Su, X.; Shi, X.; Liu, L.; Wang, T.; Xu, X.; Zhao, M.; Zhai, Y.; Yang, H. B.; Liu, B. Promoting electrochemical CO_2 reduction to formate via sulfur-assisted electrolysis. *Adv. Funct. Mater.* **2025**, *35*, 2403547.
(44) Zhang, Y.; Chen, Y.; Liu, R.; Wang, X.; Liu, H.; Zhu, Y.; Qian, Q.; Feng, Y.; Cheng, M.; Zhang, G. Oxygen vacancy stabilized $Bi_2O_2CO_3$ nanosheet for CO_2 electroreduction at low overpotential enables energy efficient CO-production of formate. *InfoMat* **2023**, *5*, e12375.
(45) Luo, Y.; Chen, S.; Zhang, J.; Ding, X.; Pan, B.; Wang, L.; Lu, J.; Cao, M.; Li, Y. Perovskite-derived bismuth with I^- and Cs^+ dual modification for high-efficiency CO_2-to-formate electrosynthesis and Al-CO_2 batteries. *Adv. Mater.* **2023**, *35*, 2303297.
(46) Li, Y.; Delmo, E. P.; Hou, G.; Cui, X.; Zhao, M.; Tian, Z.; Zhang, Y.; Shao, M. Enhancing local CO_2 adsorption by L-histidine incorporation for selective formate production over the wide potential window. *Angew. Chem., Int. Ed.* **2023**, *62*, e202313522.
(47) Ma, W.; Bu, J.; Liu, Z.; Yan, C.; Yao, Y.; Chang, N.; Zhang, H.; Wang, T.; Zhang, J. Monoclinic scheelite bismuth vanadate derived bismuthene nanosheets with rapid kinetics for electrochemically reducing carbon dioxide to formate. *Adv. Funct. Mater.* **2021**, *31*, 2006704.
(48) Ren, X.; Liu, F.; Wu, H.; Lu, Q.; Zhao, J.; Liu, Y.; Zhang, J.; Mao, J.; Wang, J.; Han, X.; Deng, Y.; Hu, W. Reconstructed bismuth oxide through in situ carbonation by carbonate-containing electrolyte for highly active electrocatalytic CO_2 reduction to Formate. *Angew. Chem., Int. Ed.* **2024**, *63*, e202316640.
(49) Xia, C.; Zhu, P.; Jiang, Q.; Pan, Y.; Liang, W.; Stavitski, E.; Alshareef, H. N.; Wang, H. Continuous production of pure liquid fuel solutions via electrocatalytic CO_2 reduction using solid-electrolyte devices. *Nat. Energy* **2019**, *4*, 776−785.
(50) Lv, X.; Liu, Q.; Wang, J.; Wu, X.; Li, X.; Yang, Y.; Yan, J.; Wu, A.; Wu, H. B. Grain refining enables mixed Cu^+/Cu^0 states for CO_2 electroreduction to C_{2+} products at high current density. *Appl. Catal. B: Environ.* **2023**, *324*, 122272.
(51) Li, H.; Wei, P.; Liu, T.; Li, M.; Wang, C.; Li, R.; Ye, J.; Zhou, Z.-Y.; Sun, S.-G.; Fu, Q.; et al. CO electrolysis to multicarbon products over grain boundary-rich Cu nanoparticles in membrane electrode assembly electrolyzers. *Nat. Commun.* **2024**, *15*, 4603.
(52) Jouny, M.; Luc, W.; Jiao, F. General techno-economic analysis of CO_2 electrolysis systems. *Ind. Eng. Chem. Res.* **2018**, *57*, 2165−2177.
(53) Bushuyev, O. S.; De Luna, P.; Dinh, C. T.; Tao, L.; Saur, G.; van de Lagemaat, J.; Kelley, S. O.; Sargent, E. H. What should we make with CO_2 and how can we make it? *Joule* **2018**, *2*, 825−832.
(54) Deng, W.; Zhang, P.; Seger, B.; Gong, J. Unraveling the rate-limiting step of two-electron transfer electrochemical reduction of carbon dioxide. *Nat. Commun.* **2022**, *13*, 803.
(55) Fletcher, S. Tafel slopes from first principles. *J. Solid State Electrochem.* **2009**, *13*, 537−549.
(56) Zheng, T.; Liu, C.; Guo, C.; Zhang, M.; Li, X.; Jiang, Q.; Xue, W.; Li, H.; Li, A.; Pao, C.-W.; Xiao, J.; Xia, C.; Zeng, J. Copper-catalysed exclusive CO_2 to pure formic acid conversion via single-atom alloying. *Nat. Nanotechnol.* **2021**, *16*, 1386−1393.
(57) Li, J.; Zeng, H.; Dong, X.; Ding, Y.; Hu, S.; Zhang, R.; Dai, Y.; Cui, P.; Xiao, Z.; Zhao, D.; et al. Selective CO2 electrolysis to CO using isolated antimony alloyed copper. *Nat. Commun.* **2023**, *14*, 340.
(58) Sun, B.; Li, Z.; Xiao, D.; Liu, H.; Song, K.; Wang, Z.; Liu, Y.; Zheng, Z.; Wang, P.; Dai, Y.; et al. Unveiling pH-dependent adsorption strength of $*CO_2^-$ intermediate over high-density sn single atom catalyst for acidic CO_2-to-HCOOH electroreduction. *Angew. Chem., Int. Ed.* **2024**, *63*, e202318874.
(59) Ni, W.; Guan, Y.; Chen, H.; Zhang, Y.; Wang, S.; Zhang, S. Molecular engineering of cation solvation structure for highly selective carbon dioxide electroreduction. *Angew. Chem., Int. Ed.* **2023**, *62*, e202303233.
(60) Sui, P.-F.; Gao, M.-R.; Feng, R.; Liu, S.; Luo, J.-Li. Unveiling phase-selective α- and β-Bi_2O_3-derived electrocatalysts for CO_2 electroreduction. *Chem. Catal.* **2023**, *3*, 100842.

https://doi.org/10.1021/acs.nanolett.5c03829
Nano Lett. XXXX, XXX, XXX−XXX